The miscibility of calcium silicate perovskite and bridgmanite: A single perovskite solid solution in hot, iron-rich regions

Joshua M. R. Muir[1*], Andrew R. Thomson[2], Feiwu Zhang[1†]

1) State Key Laboratory of Ore Deposit Geochemistry, Institute of Geochemistry, Chinese Academy of Sciences, 99 West Lincheng Road, Guiyang, Guizhou 50081, China

2) Department of Earth Sciences, University College London, London WC1E 6BT, UK.

[*] j.m.r.muir@mail.gyig.ac.cn

[†] zhangfeiwu@mail.gyig.ac.cn

Abstract

Calcium silicate perovskite and bridgmanite are two phases believed to coexist throughout the lower mantle, which at some temperature, at least theoretically, dissolve into each other to form a single perovskite solid solution ($Ca_xMg_{1-x}SiO_3$). This may have large seismic and geochemical implications due to the changes in density, elasticity and element partition coefficients between single and mixed phase perovskites. DFT Molecular Dynamics has been used to estimate the miscibility of bridgmanite and calcium perovskite at pressures between 25 and 125 GPa. At 125 GPa (where mixing is the greatest in our pressure range) to mix 1% of Ca-pv into bridgmanite requires a temperature of 2042 K, 5% 2588 K, 10% 2675 K and 50% 2743 K. Therefore, in a simplified lower mantle chemistry an extensive $MgSiO_3$-$CaSiO_3$ solid solution is not expected to occur. However, a simple model was employed to test whether the presence of other elements might influence this mutual solid solution and it was demonstrated that if sufficient concentrations (> 1 at.%) of additional elements are present then miscibility may become favourable. Of the elements likely to be present at these concentrations it appears that ferrous iron promotes, whilst aluminium inhibits, a single-phase perovskite solid solution. To a lesser extent ferric iron may both increase and decrease perovskite miscibility. Modelling for realistic mantle compositions suggests that basaltic lithologies will always retain two perovskite components, whereas a single perovskite solid solution may be preferred in

hot and/or iron-rich pyrolytic bulk compositions near the base of the lower mantle. Static calculations indicate perovskite miscibility may cause pyrolytic lithologies (with 12.5% $CaSiO_3$) to possess lower density (-0.14-0.25%), V_s (-1.5-3.5%) and V_p (-0.5-1.2%), and higher V_Φ (+0.00-0.75%) than predicted for assemblages containing two perovskites. These seismic changes, while preliminary, are similar to those observed in the LLSVPs which are also regions that are likely hotter than the surrounding mantle and thus possess conditions promoting the formation of a single perovskite phase.

1. Introduction:

At depths beyond 600-700 km perovskite (ABO_3) solutions will predominate in both ultra-mafic and mafic lithologies and control their physical attributes (Irifune and Ringwood, 1993, O' Neill and Jeanloz, 1990, Ono et al., 2004a, Hirose et al., 2017). In the lower mantle the two perovskite phases are $CaSiO_3$ (ca-pv) and $MgSiO_3$ (bdg) (Irifune, 1994). While work has been done to elucidate the seismic behaviour of both bdg and ca-pv (Hirose et al., 2017, Marquardt and Thomson, 2020) in order to understand their behaviour and effect on the lower mantle, these phases may not always exist as separate phases. $CaSiO_3$ and $MgSiO_3$ have identical chemical formulas and very similar chemical structures built around SiO_6 octahedra. Making a combined $Mg_xCa_{1-x}SiO_3$ by dissolving one phase into the other will increase configurational entropy at the A site (which contains Mg^{2+} and/or Ca^{2+}) and thus will be increasingly favoured by temperature. At low temperatures mixing between these two phases is unlikely because of the large size difference between Mg^{2+} and Ca^{2+} cations which will increase the enthalpy of mixing. At sufficiently high temperatures, however, the configurational entropy effect could outweigh the enthalpy effect and mixing could occur, such that lower mantle assemblages only possess one perovskite phase. Previous experimental studies have reported occasional lower mantle assemblages containing only one perovskite phase (for example Creasy et al. (2020), Gu et al. (2016)), which could indicate the occurrence of miscibility at high temperature. Sinmyo and Hirose (2013) observed separate Ca-pv and bdg in a pyrolytic mixture at 82 GPa and 2100 K but then did not observe Ca-pv at 109 GPa and 2300 K suggesting a dissolution of

Ca-pv into bdg between these points. Mid Ocean Range Basalts (MORB) which have similar proportions of Ca-pv and bdg and thus require high miscibility to form a solid solution have been measured up to high pressures and temperatures (89 GPa and 2400 K in Ricolleau et al. (2010), 59.2 GPa and 2750 K, 43.2 GPa and 3250 K and 101 GPa and the melting temperature in Funamori et al. (2000)) with separate Ca-pv and bdg phases measured throughout.

Since an intermediate phase would likely have different seismic properties from a mechanical mixture of the endmembers, it is essential to establish whether this two-phase chemical mixing is possible at lower mantle conditions.

The solubility of Ca into bdg and Mg into ca-pv has been studied experimentally, although these studies explicitly measuring the solubility have so far been limited to maximum temperatures of 2000 K and pressures of 100 GPa (Irifune et al., 2000, Irifune et al., 1989, Tamai and Yagi, 1989, Fujino et al., 2004, Armstrong et al., 2012). At these conditions, it has generally been found that there is only a small mutual solubility of these perovskites at lower mantle conditions (<~1.5% at 25 GPa and 2000 K rising to ~10% at 55 GPa and 2000 K). Theoretically Jung and Schmidt (2011) found the solubility of Ca in bdg to be ~0.5 % at 2000 K and 25 GPa while Vitos et al. (2006) found this solubility to be around an order of magnitude higher. In both theoretical papers solubility decreased with pressure in contrast to experimental results (Armstrong et al., 2012, Fujino et al., 2004) which identified strongly increasing solubility with pressure**.** In both theoretical and experimental cases solubility increases markedly with temperature.

From the experimental studies of Irifune et al. (2000), Fujino et al. (2004) and Armstrong et al. (2012) it is clear that Ca-pv and bdg exist as separate phases in the shallow portions of the lower mantle. The strong pressure dependence on mixing seen in Fujino et al. (2004) and Armstrong et al. (2012) suggests that at deeper and hotter portions of the lower mantle, beyond the pressures and temperatures of these experiments, a complete solid-solution may be stable as was also suggested by the results of Sinmyo and Hirose (2013). Further investigation of this potential miscibility is required to both clarify the mineral structure of perovskites at deep lower mantle conditions and to

resolve the differing predictions of theory and experiments on the pressure effect of mutual solubility.

Another factor which needs to be considered is the presence of contaminants (intrinsic defects) and their effect on phase miscibility. Both Ti (Armstrong et al., 2012) and Fe (Fujino et al., 2004) have been shown to increase the mixing of these two phases. Creasy et al. (2020) observed a single phase perovskite with a composition containing 18 ± 2 mol% $CaSiO_3$ component alongside an additional 0.59 cations of Al, Fe^{2+} and Fe^{3+} per formula unit (assuming ABO_3 stoichiometry). It is currently unclear, however, what elements are important and how big of an effect these elements have on the overall miscibility.

In this work we use Density Functional Theory (DFT) to probe the mutual solubility of Ca-pv and bdg, with and without intrinsic defects, up to pressures and temperatures corresponding to the D'' region adjacent to the core-mantle boundary (125 GPa and 3000 K). For a review of previous lower mantle theoretical calcluations see Tsuchiya et al. (2020). We built a model of Ca-pv and bdg miscibility and speculate as to whether or not this suggests a single perovskite solid solution might be stable at depth within the lower mantle. Finally, we conduct static (0 K) calculations to estimate the seismic signature of a single-phase perovskite relative to a mechanical mixture of Ca-Pv and bdg.

2. Methods

2.1 Mixing Thermodynamics

To determine whether two phases mix we determine the thermodynamic properties of the following reaction:

$$xCaSiO_3 + (1-x)MgSiO_3 \rightarrow Ca_xMg_{1-x}SiO_3 \qquad \text{Reaction 1}$$

Reaction 1 is for the pure end members. Defect elements can be introduced later by adding them to both sides of the reaction.

The Gibbs energy of this mixing reaction is defined by:

$$\Delta G_{mix} = \Delta H_{mix} - T\Delta S_{mix} \qquad \text{Equation 1}$$

where ΔH_{mix} is the enthalpy of mixing, T is the temperature, ΔS_{mix} is the entropy of mixing and ΔG_{mix} is the free energy of mixing. Mixing will occur when ΔG_{mix} is negative. ΔS_{mix} is broken into two components ($\Delta S_{mix} = \Delta S_{vib} + \Delta S_{config}$); ΔS_{vib} represents the vibrational entropy and ΔS_{config} represents the configurational entropy. ΔG_{mix} will subsequently be determined in two parts. S_{vib} will be determined using molecular dynamics and ΔH_{mix} and ΔS_{config} will be determined using static calculations.

Calculations were performed across a wide range of discrete *PT* conditions and interpolated to create a model covering conditions throughout the lower mantle. Molecular dynamics calculations were run at 25, 75 and 125 GPa and temperatures of 1000, 2000 and 3000 K. Energies were determined at Ca#=0, 0.25, 0.50 and 1 where Ca# is Ca/(Ca+Mg) in the entire system. For a 2-perovskite phase assemblage Ca# defines the relative phase proportion of $CaSiO_3$ expected. Static calculations (used to determine ΔH_{mix} and ΔS_{config}) were performed with Ca# of 0, 0.125, 0.25, 0.5, 0.75, 0.875 and 1 and at pressures of 25, 75 and 125 GPa (additional pressures for ΔH_{mix} are shown in Table S2). All pressures are presented uncorrected, see the supplementary methods for more information.

To calculate G_{mix} at specified *T*, *P* and *Ca#* we used the following scheme. First at each pressure (25, 75 and 125 GPa), temperature (1000, 2000 and 3000 K) and Ca# (0, 0.25, 0.5 and 1) we calculated *G* of the products and the reactants. Polynomials were fitted to the change in ΔG_{mix} as a function of Ca# (e.g. Figure S1) followed by pressure at each temperature. Application of these functions allows calculation of ΔG_{mix} at any given Ca# and pressure. Subsequently, polynomials were fitted as a function of T (a sample is shown in Figure S2) to determine the ΔG_{mix} of the reaction at the T of interest. The fits across P and T are relatively linear and are likely reliable at middling Ca# values where there are large energy differences between the mixed and unmixed components and where mixing is controlled by configurational entropy which is well constrained by the Boltzmann entropy. Energy varies strongly as a function of Ca# and inaccuracies in Ca# extrapolation could lead to large errors in G_{mix}. The G of the points at Ca#=0.25 fit near exactly to a curve of G vs Ca# plotted with

131 points at Ca#=0, 0.5 and 1 as shown in Figure S1 which suggests that a polynomial fit of G vs Ca# is
132 adequate. This fitting likely breaks down at extremely high and low Ca# values which is important for
133 harzburgite but as shown in Table S1 a solid solution model returns near identical answers and the
134 errors implicit in the molecular dynamics calculations appear to dominate.

135 *2.2 Computational Details*

136 For these calculations we used the VASP code version 5.4.4 (Kresse and Furthmuller, 1996b,
137 Kresse and Furthmuller, 1996a). This is a density functional theory approach where planewave
138 pseudopotentials are used to simulate supercells which represent infinite crystals. The PBE (Perdew
139 et al., 1996) exchange correlation functional was used alongside the included VASP PAW potentials
140 (Kresse and Joubert, 1999). The valence electron shells used were Ca: 3s, 3p, 4s; Mg 3s, 3p; Si 2s, 2p;
141 O 2s, 2p. Two different sets of calculations were performed, both at static conditions and using
142 molecular dynamics. Static calculations had planewave cut-offs of 850 eV and k-point grids of 4x4x4
143 in a Monkhorst Pack grid (Monkhorst and Pack, 1976). Energies were relaxed to within 10^{-5} eV and
144 forces between atoms were relaxed to below 10^{-4} eV/Å. For molecular dynamic runs the gamma
145 point was used with cut-offs of 600 eV and relaxed to within 10^{-4} eV**.** 80 atom unit cells were used
146 (2x2x1) for *Pbnm* and *I*4/*mcm* structures and 40 atom unit cells (2x2x2) for $Pm\bar{3}m$ structures, except
147 for during calculation of the configurational entropy as noted below. Elasticity constants were
148 calculated using the stress-strain method on 80 atom unit cells and static conditions using the same
149 cut-offs as listed above (more details in the supplementary methods).

150 *2.3 Phases:*

151 $MgSiO_3$ is usually in the orthorhombic *Pbnm* structure (Zhang et al., 2013). There is much debate
152 about the crystallographic structure of $CaSiO_3$ in the lower mantle (e.g. Stixrude et al. (2007), Sun et
153 al. (2014), Shim et al. (2002), Ono et al. (2004b), Uchida et al. (2009), Komabayashi et al. (2007) and
154 Kurashina et al. (2004)), but following Stixrude et al. (2007) and Sun et al. (2014) we assume $CaSiO_3$
155 possesses either the cubic $Pm\bar{3}m$ or the tetragonal *I*4/*mcm* structures. For more discussion of
156 $CaSiO_3$ phases see the supplementary methods. All systems (end members and mixtures) were

calculated in all 3 of these symmetry groups. Interpolations across Ca# and temperature were done for all 3 symmetry groups and then at any specific composition and temperature point the lowest energy structure was chosen. For Mg end members the *Pbnm* phase dominated, whereas the *I*4/*mcm* or $Pm\bar{3}m$ phases were dominant for Ca end members, with the $Pm\bar{3}m$ phase favoured by high temperatures. The single-phase solid solution perovskite generally adopted the *Pbnm* structure with this always being adopted when Ca#=0.25 or 0.5. This preference for a *Pbnm* structure in the mixed phase is consistent with previous experimental and theoretical observations of Armstrong et al. (2012) and Jung and Schmidt (2011) respectively**.**

To test whether post-perovskite phases were promoted by phase mixing, calculations were run on a mixed phase with a *Cmcm* structure and Ca#= 0.5 at 125 GPa but this post perovskite phase was found to be higher in energy than the *Pbnm* phase at all tested temperatures (1000, 2000 and 3000 K).

2.4 Molecular Dynamics:

To determine the vibrational entropy of each system a Velocity-Autocorrelation Function (VACF) method was used. More accurate methods, e.g. thermodynamic integration, are possible but because ΔG_{mix} values are fairly large in magnitude the accuracy of these methods was presumed to be unnecessary. Details of this are given in the supplementary information.

All molecular dynamics runs were performed on 80 atom (2x2x1) cells (for *Pbnm* and *I*4/*mcm*) or 40 atom (2x2x2) cells for $Pm\bar{3}m$ structures. To ensure these cell sizes were sufficient for convergence to be achieved, additional tests were also run a test on larger cells at 125 GPa and 2000 K; a 160 atom cell (2x2x2) for *Pbnm*-structured $MgSiO_3$ and $Mg_{0.5}Ca_{0.5}Si0_3$ and a 160 atom (2x2x2) cell for *I*4/*mcm*-structured $CaSiO_3$. The differences in energy between 80 atom and 160 atom unit cells were < 0.40 meV/atom for $MgSiO_3$, < 0.51 meV/atom for $Mg_{0.5}Ca_{0.5}Si0_3$ and < 0.58 meV/atom for $CaSiO_3$. Overall, this corresponds to a change of less than 0.51 meV/atom in ΔG_{mix} for reaction 1, implying that good convergence is achieved using 80 atom unit cells.

The error in the energies obtained using molecular dynamics were calculated for each individual run using the method of Flyvbjerg and Petersen (Flyvbjerg and Petersen, 1989), and were less than 1.5 meV/atom in all cases. The effect of propagating these errors is explored in Table S1 but we find that within 2σ T_{mix} does not vary by more than 50 K for any Ca#.

2.5 Configurational Entropy:

To determine the configurational entropy of perovskite solid solutions we calculated the energy of different configurations of Mg and Ca in the unit cell. As the number of possible configurations are proportional to N factorial, 80-atom cells are too large to test all possible configurations. However, the energy difference of each configuration is independent of the simulation cell size, such that the only disadvantage of using a smaller simulation cell when determining configurational entropy is that some configurations may be somewhat under- or over-sampled. A smaller simulation cell consisting of 40 atoms (2x2x1 unit cells) for compositions with x=0.25, 0.5 and 0.75 (for $Ca_xMg_{1-x}SiO_3$) will not contain every configuration that would be assessed using an 80 atom simulation cell, however, it does contain a sufficiently large number of configurations such that the configurational entropy in an infinite crystal is adequately approximated. For solid solutions with x=0.125 or 0.875 use of an 80 atom simulation cell was required to ensure sufficient unique configurations were probed. Thus we used a 40 atom cell for x=0.25, 0.5 and 0.75 and an 80 atom cell for x=0.125 and 0.875. For each of these cells we calculated the enthalpy for every possible configuration of Ca and Mg in the cell and calculated the configurational entropy using the Gibb's entropy function with details given in the supplementary methods. Our method likely underestimates the configurational entropy but as explained in the text using the maximum possible configurational entropy (the Boltzmann entropy) makes little difference to our results. This means that the deviation of calculated entropy from the perfect Boltzmann entropy value is not a significant control on the miscibility and any underestimation of configurational entropy is not a significant control on our results.

208

209 ## 3. Results:

210 *3.1 Enthalpy and Entropy of Mixing*

211 The miscibility of any two endmembers can be assessed using Equation 1, which evaluates the
212 change in Gibbs energy (ΔG_{mix}) were full miscibility to occur. For any two substances ΔS_{mix} will be
213 positive, since a single miscible solid-solution will always have more available atomic arrangements
214 than two coexisting endmembers. Assuming that the two endmembers are naturally immiscible at
215 low temperature, ΔH_{mix} is also positive because energy is required to overcome their natural
216 aversion to mixing. As the reaction occurs when ΔG_{mix} is negative, miscibility can be achieved with
217 increasing temperature as $-T\Delta S_{mix}$ overcomes the positive ΔH_{mix}, providing this occurs prior to
218 melting or dissociation of the original endmember phases. Mutual solubility of the two endmembers
219 occurs at thermodynamic equilibrium, when $\Delta G_{mix} = 0$, at a temperature subsequently denoted T_{mix}.
220 The temperature T_{mix} defines the maximum extent of the two-phase solvus.

221 The values of ΔH_{mix}, ΔS_{config} and ΔS_{vib} calculated as described above are reported as a function of
222 pressure in Tables S2, S3 and S4 respectively. Inspection of these parameters reveals that ΔH_{mix}
223 increases with pressure, ΔS_{config} only slightly increases and is almost insensitive to pressure increases
224 and ΔS_{vib} has a complex relationship but generally increases with pressure. The increase in ΔH_{mix} with
225 pressure occurs despite the single perovskite solid solution being less dense than a mechanical
226 mixture of the two phases (Table 1). This is likely due to the energy required to replace Mg^{2+} with
227 larger Ca^{2+} cations, which increases with pressure as the perovskite A-site is compressed.

228 Combining the pressure systematics of ΔH_{mix}, ΔS_{config} and ΔS_{vib} demonstrates that increases in
229 ΔH_{mix} are overcome by growth in the entropy terms at high pressure, such that T_{mix} is observed to fall
230 as pressure increases (Figure 1). This observation is consistent with the results of Fujino et al. (2004)
231 and Armstrong et al. (2012). Inspection suggests that it is the increasing magnitude of ΔS_{vib} that is
232 responsible for Equation 1 becoming more negative and promoting a single perovskite solid solution
233 with pressure. This is in contrast with two previous theoretical studies, which both concluded that

234 T_{mix} should increase with pressure (Jung and Schmidt, 2011, Vitos et al., 2006). However, as both
235 these studies only estimated ΔS_{vib} without calculating it, the increase in T_{mix} with pressure and the
236 high values for T_{mix} (> 4000 K) obtained within these studies appear to have been caused by poor
237 constraint on the value and the changes in ΔS_{vib} with pressure.

238 Calculated values for ΔS_{config} vary slightly from ideal Boltzmann entropy values, but this effect is
239 small. If we were to replace all ΔS_{config} values with those of an ideal Boltzmann mixture, T_{mix} would
240 vary by less than 75 K in all cases (less than 10 K in most occurrences). Thus, it is concluded that Ca
241 and Mg are largely interchangeable between various different sites such that ideal mixing, as far as
242 configurational entropy is concerned, occurs.

243 *3.2 Mixing in the $CaSiO_3$-$MgSiO_3$ system:*

244 Figure 1 plots the calculated $MgSiO_3$-$CaSiO_3$ solubility as a function of temperature at pressures
245 of 25, 75 and 125 GPa (an alternative rendering as a phase diagram is shown in Figure S3). At each
246 pressure we identify two regions in the miscibility loop structure. At low, or high, Ca# (at 125 GPa
247 Ca# <~0.1 or >~0.9) the miscibility boundary changes rapidly with the temperature in response to
248 the control of ΔH_{mix} and ΔS_{vib}. At intermediate Ca# values (at 125 GPa Ca# between ~0.1-0.9), the
249 miscibility curve plateaus, and there is little continuing change with temperature as this region is
250 controlled by ΔS_{config}.

251 In the $CaSiO_3$-$MgSiO_3$ system the calculated solubilities of Ca in bdg and Mg in ca-pv at 25 GPa
252 and 2000 K are ~ 0.41% and ~ 0.18% respectively, while T_{mix} at Ca#=0.5 (the temperature required
253 for complete solid solution) is ~ 3170 K. At 75 GPa the calculated solubilities at 2000 K increase to ~
254 0.52 and ~ 0.13% respectively, with T_{mix} at Ca#=0.5 falling to ~ 3050 K. At 125 GPa the calculated
255 solubilities at 2000 K are ~ 1.12 and ~ 0.07% respectively, with T_{mix} at Ca#=0.5 ~ 2740 K. At 2000 K
256 increasing the pressure thus has little effect on solubility. At higher temperatures increasing the
257 pressure causes a large increase in solubility. This high temperature effect is due to the different
258 plateau temperatures seen in Figure 1. In the theoretical study of Jung and Schmidt (2011) the

259 solubility of Ca in bdg was found to be 0.5% and the solubility of Mg in Ca-pv to be much lower at 25
260 GPa and 2000 K which is similar to our work.
261 Experimentally Fujino et al. (2004) found solubilities of ~ 1% Ca in bdg and 4% Mg in ca-pv at 2273 K
262 and 30 GPa, Irifune et al. (2000) found 1.1-1.5% solubility of Ca in bdg and 2.1-3.2% of Mg in Ca-pv at
263 25 GPa and 1973 K and Armstrong et al. (2012) found 4.7% solubility of Mg in Ca-pv at 53 GPa and
264 2000 K. These experimental results all show higher solubility than we predict here. Small solubilities
265 are the hardest to constrain as they occupy the steepest part of Figure 1. Differences between our
266 predictions and experiments could arise either through problems with our fitting model which
267 extrapolates down to low Ca# numbers or through inaccuracies in our calculations. As shown in
268 Table S1 a Margules fitting model provides the same result as our polynomial fit but more fitting
269 parameters at lower Ca# could possibly change this outcome. At these low solubilities the main
270 constraint, however, is not fitting but the small energies involved. The difference between a
271 solubility of 0.41% (predicted by us) and 1.25% at 2000 K and 25 GPa (measured by Irifune *et al.*
272 2000) is a shift in the energy of R1 of less than 1 meV/atom. This is beginning to approach the limits
273 of MD accuracy particularly without very long and costly calculations. The difference in solubility
274 between experiment and our calculations are likely to be much larger at small solubilities where the
275 mixing curve is steep (Figure 1) than at large solubilities on the order of mantle phase compositions
276 where the mixing curve flattens out and small energy differences in mixing are unimportant. Thus at
277 lower mantle conditions our solubilities should be better constrained. Experimentally there could be
278 thermal lags across the system, particularly at interfaces of mixing where heat may not transfer well.
279 If experimental temperatures at the mixing interface are higher than recorded in the sample that
280 could also explain these differences in solubility. Different experiments use different pressure scales
281 (Armstrong *et al.* (2012) and Fujino *et al.*(2004) use ruby fluorescence, Irifune *et al.* (2000) Au) and
282 the calibration of these can sometimes lead to significant differences (see for example Ye et al.
283 (2018)) which may cause additional differences. Our pressures in this study are uncorrected for the
284 systematic pressure errors in DFT which could lead to a shift of over -5 GPa. Compositional

differences between experimental samples could also lead to solubility differences which shall be explored in the next section. Finally, another possible source of difference comes from the definition of solubility. Our study defines solubility by its thermodynamic equilibrium with no consideration of kinetics whereas the experimental studies define solubility by the disappearance of XRD or ATEM patterns. This experimental definition allows for the presence of metastable dissolutions and problems with detection limits, both of which should increase measured solubility in the experimental case.

3.3 The Effect of Other Elements

The chemical complexity of the natural mantle means that Ca-pv and bdg are likely to contain many intrinsic defect elements when stable at lower mantle conditions. Bridgmanite crystals have been shown to be capable of hosting large (1-10 at. %) amounts of Fe and Al (Kaminski, 2017) alongside smaller quantities of several additional elements. Any additional elements, even those present in extremely small amounts, can have a large effect on ΔS_{config}, whereas only elements present in large amounts will have significant effects on ΔH_{mix} and ΔS_{vib}. As there was no conceptual model for which elements will most significantly affect the thermodynamic parameters for perovskite solubility we have employed a simple defect model allowing the effect of incorporating a large number of elements (Table 2) to be examined at 25 and 125 GPa in a bulk composition with Ca#=0.1 (a roughly pyrolytic assemblage). Our method and its assumptions are outlined more fully in the supplementary methods but in essence we calculate the change to H_{mix} from adding 1 defect to 80 atom unit cells, assume that defect induced changes to H_{mix} are linear, defect induced changes to S_{config} can be described by the Bolzmann entropy equation and that defect induced changes to S_{vib} are unimportant. This is a crude method with multiple large assumptions but as shown in Table S5 should capture the rough magnitude of defect induced changes to T_{mix} allowing us to identify which elements are important and in what concentrations they are important.

Table 2 demonstrates that there is no clear pattern, with charge or ionic size, for which defect elements are most likely to alter T_{mix} such that individual electronic effects must be dominating the

311 estimated results. Therefore, it is difficult to predict off-hand which elements will affect T_{mix}
312 significantly and in which sense. Whilst many elements increase T_{mix} others reduce ΔH_{mix} and thus
313 also T_{mix}. The most important of those which reduce T_{mix} are the noble gases (which can cause very
314 large reductions of H_{mix} due to their position as an interstitial defect). Na(I), K(I), many of the
315 transition metals in particular Co(II), Ni(II) Sc(II) and Fe(II), and 4+ cations that replace Si such as S, Ti
316 and C also reduce the temperature of miscibility. Some elements that strongly increase H_{mix} and thus
317 T_{mix} are the larger alkaline earth metals (Sr, Ba) and B. Increasing the pressure has varied effects on
318 these trends, increasing H_{mix} for some elements and decreasing it for others, but defect induced Δ
319 T_{mix} values are similar at 25 and 125 GPa. This is because the largest effect of defect elements on T_{mix}
320 is through modifying S_{config} which in this model is pressure independent. Even though defect changes
321 to H_{mix} (ΔH_{mix}) are very significant, pressure induced changes to ΔH_{mix} are largely insignificant
322 compared to S_{config}. We note that whilst we have estimated the effect of many elements on
323 perovskite miscibility we have not explicitly calculated the solubility of each of these defects in the
324 solid solution at mantle conditions and thus the predicted effects are meant to serve as illustrative.
325 The most notable observation from this modelling is that large amounts of defects are required
326 to induce significant changes in T_{mix}. With Ca#=0.1, all defect atoms require a concentration greater
327 than 0.3 atomic% for T_{mix} to change by 100 K, with the required concentrations in excess of 1 atomic %
328 for most elements. This is significant because most defects atoms which can be incorporated in bdg
329 and Ca-pv are likely to be well below this level, allowing restriction of the elements under
330 consideration to those that are significantly abundant in the bulk mantle composition or those
331 thought to be concentrated in certain regions. Throughout the remainder of this study we assume
332 that the only elements likely to be significantly abundant to alter perovskite miscibility substantially
333 are Fe and Al. High spin ferrous Fe was estimated to decrease T_{mix} by up to 1000 K (Fe%=10, Ca#=0.1)
334 in a pyrolytic mixture which is consistent with the observation of Fujino et al. (2004) that additional
335 iron increased the total solubility at a fixed temperature. In contrast Al appears to increase T_{mix} by up

to 230 K (Al%=5, Ca#=0.1) and so somewhat counteracts the effects of ferrous iron. The presence of Al can also promote the oxidation of iron, by forming Fe-Al pairs where the iron exists as high spin on (primarily) the A site (Shim et al., 2017, Catalli et al., 2011, Kupenko et al., 2014). With the introduction of Fe-Al pairs T_{mix} is largely unaffected with T_{mix} slightly reducing by 38 K with Fe-Al%=5 and Ca#=0.1. Pure ferric iron (as a coupled substitution of two iron atoms replacing Mg-Si) only slightly decreases T_{mix} at low pressure and slightly increases it at high pressure.

The effect of these elements on some non-pyrolytic mixtures (i.e. varying Ca#) are shown in Table S6 and S7. At Ca# of 0.5 the effects of defect elements are typically reduced, such that the change in T_{mix} (ΔT_{mix}) is roughly half of what it would be in an equivalent pyrolytic system. The effect of defect elements in bulk compositions with high Ca# is similar to those with Ca#=0.1 (i.e. pyrolite), although the magnitude of defect element effects are slightly larger.

4. Discussion:

4.1 Single phase regions of the lower mantle

The composition of the lower mantle remains uncertain, and possible variations of Ca# are significant. Pyrolytic compositions are generally taken to possess a Ca# of 0.07-0.12 (Kesson et al., 1998, Irifune and Tsuchida, 2007, Mattern et al., 2005, Ringwood, 1991), whereas depleted harzburgitic rocks have far lower Ca# of 0.01-0.03 (Ringwood, 1991, Michael and Bonatti, 1985). Mafic lithologies, such as subducted mid-ocean range basalt (MORB), are the most Ca-enriched of the commonly considered mantle lithologies, possessing Ca# of between 0.3-0.6 (Hirose et al., 2005, Hirose and Fei, 2002, Irifune and Tsuchida, 2007, Ricolleau et al., 2010). These variations in bulk composition control the degree of miscibility required for a single-phase perovskite solid solution to form at lower mantle conditions. The required values of T_{mix} applicable to the compositional ranges of pyrolitic, harzburgitic and MORB bulk compositions are plotted in comparison with a mantle geotherm (Ono, 2008) in Figure 2. In defect-free pyrolytic or MORB compositions, the small

variations in the possible Ca# values do not substantially alter T_{mix}. T_{mix} for the most Ca-enriched and Ca-depleted pyrolytic compositions only vary by a maximum of 30 K, whereas T_{mix} for MORB compositions varies by < 5 K across the possible Ca# range. Due to the lower Ca-content of depleted harzburgitic mantle lithologies, small changes in the exact Ca content of the bulk composition cause significant changes in the predicted miscibility temperature according to the model employed here; e.g. T_{mix} values for Ca#=0.01 and Ca#=0.03 differ by 320 K at 25 GPa. These large differences arise because Ca# values for harzburgite occur in the region of the phase diagram where steep changes in solubility are observed, whereas those for pyrolite and MORB occur closer to the plateau regions (Figure 1). We caution that the miscibility boundary is poorly constrained at extreme values of Ca#, such that the apparent values of T_{mix} for harzburgitic compositions may be subject to significant uncertainty.

4.2 Pyrolitic Compositions

As shown in Figure 2 for a pure pyrolytic composition with no additional elements we see that T_{mix} remains above the lower mantle geotherm up until the D'' at 125 GPa. Thus, pure $CaSiO_3$ and $MgSiO_3$ are not expected to form a single perovskite solid-solution at conditions of the "normal" mantle geotherm.

Figure 3 shows the predicted effect on T_{mix} of the presence of Fe and Al compositional defects by plotting the depth in the mantle that a single perovskite solid solution is predicted to become favourable along a mantle geotherm (an alternative rendering of this graph showing T_{mix} at different pressures is provided in Figure 4 and compositional variation is shown in Figure S4 and S5). Increasing the amount of Ferrous iron increases perovskite miscibility and promotes a single-phase perovskite solid solution to become stable at shallower conditions. However, the contrasting effect of Al decreasing perovskite miscibility means that for most reasonable pyrolytic compositions T_{mix} will not be strongly affected. These predictions have assumed that the formation of Fe-Al pairs is favoured over ferrous iron and Al-Al pairs (Mohn and Tronnes (2016)). Alternatively, if ferrous iron and Al-Al pairs dominate then the predictions are somewhat different, with miscibility expected at

387 slightly shallower conditions (Figure S4). Sinmyo and Hirose (2013) observed in a pyrolytic
388 composition a disappearance of a Ca-pv phase between 82 GPa at 2100 K and 109 GPa at 2300 K.
389 The Ca# and Fe# of these samples vary between experiment/measurement but using a Ca# of 0.177
390 and a Fe% of 4 which roughly represents their values we predict T_{mix} to be 2578 K at 82 GPa and
391 2328 K at 109 GPa. Thus we predict at 82 GPa the mixing temperature to be far above the
392 experimental temperature and no mixing should occur but at 109 GPa the mixing temperature is
393 only 28 K above the experimental temperature. In this latter case mixing could occur with only slight
394 variations in temperature or iron concentration and thus our results agree with those observed by
395 Sinmyo and Hirose (2013).
396
397 While perovskite miscibility is predicted to be unfavourable in the "normal" pyrolytic mantle, hot
398 regions such as within mantle plumes or Large Low Velocity Shear Provinces (LLSVPs), may promote
399 formation of a single miscible perovskite solid solution. Figure 3 and Figure 4 plots the predicted
400 perovskite miscibility depth along a temperature profile that is 500 K above the regular mantle
401 geotherm, which may represent conditions occurring in LLSVPs or plumes (McNamara, 2019). At
402 these excess temperatures, miscibility of the endmember perovskite phases is more extensive and is
403 predicted to be favourable at pressures beyond ~ 80 GPa. Therefore, it is suggested that
404 anomalously hot peridotitic regions of the mantle may possess a phase assemblage consisting of
405 only one-perovskite and ferropericlase.
406 Model predictions therefore suggest that perovskite miscibility is promoted by excess heat and
407 high iron contents. In the natural mantle the formation of such iron-rich perovskite compositions
408 may be limited by preferential partitioning of iron into coexisting ferropericlase. Predictions plotted
409 in Figures 3-4 (and all similar graphs) refer exclusively to the concentration of defect elements in the
410 perovskite phases (bdg, Ca-pv and mixed phase) which are not equivalent to the bulk composition as
411 we have not accounted for the influence of periclase. Under normal conditions iron preferentially
412 partitions into periclase relative to bdg (Muir and Brodholt, 2016, Xu et al., 2017), with value of K_D^{pv-}

413 ^{fper} < 0.5 in the deepest portions of the mantle ($K_D^{pv\text{-}fper}$ = $[Fe_{pv}/Mg_{pv}]/[Fe_{fp}/Mg_{fp}]$. With increasing
414 pressure iron favours ferropericlase such that beyond ~80 GPa the iron in bdg is likely << 5 % Fe
415 whereas Al should remain relatively constant >~5 %. Thus, in the normal deep lower mantle iron
416 concentration in bdg should be limited relative to Al, such that T_{mix} values should remain near their
417 defect-free values or be somewhat increased. However, the mixed perovskite phase also favours Fe,
418 and will compete with ferropericlase for iron which would raise the effective iron concentration in
419 bdg for considering miscibility. More data is needed to examine this point fully but in general Fe
420 concentration in bdg in the lower mantle, even in iron-rich regions, is low, such that hot lower
421 mantle regions may be the primary source of mixed perovskite phases.
422
423 One area of the mantle that potentially is compositionally heterogeneous are the LLSVPs
424 (McNamara, 2019). While it is unclear what the compositional difference of these regions are, as
425 shown in Table 2 only differences that exceed ~1 atomic% are important to mixing of the perovskites,
426 and it remains likely that LLSVPs do not contain any defect elements at such elevated concentrations
427 other than Fe or Al. When considering LLSVPs, miscibility of the two perovskite phases should
428 primarily be constrained by their elevated temperature, with a secondary effect for potential
429 changes in Fe and Al content. Any exotic compositional differences that may exist are unlikely to be
430 important for phase mixing of the perovskite. As LLSVPs are believed to be considerably hotter than
431 the rest of the mantle they are more likely to possess a miscible perovskite solid solution.
432
433 Another area where this mixing behaviour is potentially important is in the formation of a post-
434 perovskite (ppv) phase in bdg and hence on the D''. As the pressure increases beyond 125 GPa the
435 free energy of the single chemically mixed phase (Ca-pv+bdg) becomes lower than the free energy of
436 the mechanically mixed ca-pv+bdg phases which will stabilise $MgSiO_3$ in a mixed perovskite phase
437 against the post-perovskite phase. We estimate the magnitude of this effect (see supplementary
438 results for details) and predict that for a pyrolytic mixture (Ca#=0.1) the addition of Ca-pv stabilises

439 the pv phase bdg perovskite structure against the ppv phase by ~2.75 GPa (at 125 GPa and 2700 K)
440 which would push the reaction deeper with more Ca. This is a small effect when compared to that of
441 elements like Al which can change this reaction by ~ 10 GPa (Grocholski et al., 2012).
442
443 *4.3 Harzburgitic Compositions*
444 As shown in Figure 2 harzburgitic compositions behave largely like pyrolytic compositions but
445 they have smaller values of T_{mix}, and should therefore become miscible at shallower depths. Varying
446 the Ca# ratio has a very large effect on T_{mix} in harzburgite because the possible Ca# values exist in an
447 even steeper range of the solubility curve and thus the amount of Ca that is present is extremely
448 important for determining the likelihood of mixing. The effect of other elements on harzburgite
449 mixing is shown in Figure S6 and S7 but are similar to pyrolite in that ferrous Fe increases mixing
450 sharply.
451 *4.4 Basaltic Compositions*
452 A final case to consider is a descending slab or mechanically mixed mantle with containing a
453 more MORB-like composition. As is shown in Figure 2 this has quite different behaviour to the
454 pyrolytic case. T_{mix} is considerably higher in the MORB case and is considerably above the
455 temperature of descending slabs (the temperature of MORB in a descending slab should be between
456 the coldest slab adiabat shown in Figure 2 and the geotherm with MORB generally on the outer layer
457 of slabs and thus considerably hotter than the adiabat). Varying the Ca# ratio has little effect on
458 mixing in basaltic compositions as they exist in the plateau region of Figure 1 and thus all basaltic
459 compositions should behave largely similarly. The effect of defect elements is shown in Figure S8-S9.
460 Even with extremely enriched amounts of ferrous iron (20%) T_{mix} remains nearly 600 K above the
461 temperature of the coldest adiabat at 125 GPa and thus phase mixing does not occur in descending
462 slabs even in cases of extreme iron enrichment. MORB that exists at geotherm temperatures (for
463 example from unmixed pyrolite or the extreme edges of slabs) will also not mix except in the

presence of large amounts of ferrous iron (>5%) with little Al which is unlikely as basalts are generally high in Al.

While we predict no mixing in the lower mantle for MORB our predicted mixing temperatures for MORB contradict an experimental study where MORB was heated until it melts at varying pressures up to CMB pressures and no sign of phase mixing was observed in the XRD spectra (Pradhan et al., 2015). While this sample contains large amounts of Al which will increase T_{mix} our predicted T_{mix} is still well below the melting temperature at high pressure. In this study samples were heated for 30 minutes which is similar to the heating times for experiments where mixing has been observed (Armstrong et al., 2012, Fujino et al., 2004, Irifune et al., 2000). This suggests generally that mixing had enough time to occur in these melting experiments and that the lack of any mixed phase formation was not a kinetic effect. One possible solution to this is the large amount of Fe and Al in this system, combined with a middling Ca# number, significantly slows mixing as mixing requires diffusion of all the cations (Fe, Al, Ca, Mg and Si) and cationic diffusion in bridgmanite is slow (Ammann et al., 2009) and it is likely slow in Ca-pv as well. Alternatively, our simple model may underestimate the effect of some elements, most likely Al, in raising T_{mix} and the full effect of these elements needs to be modelled with MD or experimentally. In a MORB composition Ricolleau et al. (2010) saw the persistence of 2 separate perovskite phases up to 89 GPa and 2400 K and Hirose et al. (2005) saw the presence of separate 2 separate up to 130 GPa and 2290 K. We also predict separate phases and no mixing at these points ($T<T_{mix}$).

4.5 Seismic Effects

The calculations presented above suggest that bdg and ca-pv may become miscible in hot and/or chemically anomalous regions of the deep lower mantle. If such miscibility occurs the seismological properties of the single-phase perovskite solid solution may be significantly different to that of a two-perovskite phase assemblage, such that is instructive to consider whether miscibility will alter the geophysical signature of these mantle portions.

489 The density of a single-phase perovskite solid solution of pyrolytic composition is compared with
490 that of a mechanical mixture of bdg and ca-pv in Table 1. A single perovskite solid solution is less
491 dense than an equivalent mechanical mixture, but this density difference is small (<0.26%) and
492 therefore unlikely to have large effects without associated changes in the bulk and/or shear moduli.
493 In Figure 5 we consider the elasticity of these structures.
494 These considerations are not completely straightforward as, firstly, throughout several studies
495 published across the literature the elasticity of the Ca-pv phase has proven to be difficult to
496 determine, using both theoretical and experimental techniques (Thomson et al., 2019, Kawai and
497 Tsuchiya, 2015). Secondly, all considerations of perovskites' elasticities need to include possible
498 temperature variations within different regions of the mantle, especially those that are most likely to
499 be relevant to perovskite miscibility. Thirdly, the geophysical elasticity of a mechanical mixtures of
500 ca-pv and bdg will depend upon the geometry of each component in the mixture, and without
501 precise knowledge of these details any estimates will have large uncertainties. In spite of these
502 difficulties the difference in elasticity between miscible one-perovskite and a mechanically mixed
503 two-phase assemblage are estimated using static calculations (at 0 K) by adopting two major
504 approximations. The first approximation is that all errors associated with the calculation of ca-pv's
505 velocities (which remain unknown) cancel when considering only the velocity difference between
506 Ca-pv+bdg and a miscible perovskite. This assumption is justified by the observation that both sides
507 of the reaction contain CaO_{12} dodecahedrons, such that any errors resulting from calculations of
508 their elasticity are nullified. The second approximation is that the changes in elasticity induced by
509 phase miscibility occur primarily via changes to the static bulk (K) and shear (G) moduli, and that high
510 temperature phonons do not cause large relative changes to K or G. As shown in Table 1, static
511 calculations predict a density change resulting from miscibility that is close to an average of high
512 temperature results, such that it is not unreasonable to assume this assumption is justified. To
513 assess the third difficulty, that the geometry of mechanical mixtures of bdg and ca-pv remain
514 unknown, it is assumed that the Hashin-Shtrikman bounds provides the maximum and minimum

possible values of elasticity variations (Hashin and Shtrikman, 1963). The one-phase miscible perovskite assemblage has no bounds, but its elasticity is compared with the upper and lower bounds of the two phase mixture of bdg + ca-pv (Figure 5) so that the true elasticity difference must lie between these bounds.

Employing these approximations a pyrolytic miscible one-phase perovskite (Ca# = 0.125) possesses lower shear and compressional wave velocities ($-1.5 > \Delta V_s > -3.5\%$, , $-0.5 > \Delta V_p > -1.2\%$) but a higher bulk sound speed ($0 < \Delta V_\Phi < 0.75\%$) compared to a two-phase mechanical mixture (Figure 5). These velocity differences are potentially seismically relevant, possessing a similar magnitude to those observations made within the LLSVPs, where a drop in V_s of 1-5% is associated with little density variation and a possible anticorrelation of V_s-V_Φ (McNamara, 2019, Koelemeijer et al., 2017)**.** The magnitude of the predicted velocity variations increase with increasing Ca# at 125 GPa (Figure 6), such that ΔV_s and ΔV_p become more negative whilst ΔV_Φ increases. As Ca# appears to exert a strong control on predicted velocity differences, compositions more enriched in calcium would possess a larger seismic signature associated with perovskite miscibility if it occurs.

Whilst these static calculations provide some indication of the possible geophysical signature of miscibility, stronger conclusions require further calculations to be performed at high temperature and additional support for the assumptions we have made. Due to the difficulties in simulating and measuring the elasticity of ca-pv, this may require dedicated high precision calculations or appropriate experimental studies.

5. Conclusion

In this work we observe that ca-pv and bdg are unlikely to become miscible at conditions of the lower mantle geotherm. At pressures of 25, 75 and 125 GPa we find the solubility of Ca in bdg to be 0.41/0.52/0.92 % at 2000 K and 0.72/1.07/3.30 % at 2500 K within the pure $MgSiO_3$-$CaSiO_3$ binary system. Complete perovskite miscibility is potentially possible within pyrolytic bulk compositions

near the base of the mantle (> 90 GPa) in regions where temperatures are elevated, such as in an LLSVPs. Descending slabs should possess two perovskite phases across all reasonable mantle conditions.

Perovskite miscibility may lead to small density decreases alongside seismically significant changes of the shear wave speed when predictions for a single-phase perovskite solid solution are compared with 2-perovskite mechanical mixtures. Additionally, our static calculations suggest an anticorrelation of shear wave velocity and bulk sound speed may occur in regions where miscibility is favourable. These predicted elasticity changes are similar to those observed within the LLSVPs, which are also believed to be regions that possess super-adiabatic temperatures. Since regions of elevated temperature are predicted to be those most likely to favour perovskite miscibility it is feasible that this provides some explanation for the anomalous geophysical properties of these regions of the deep mantle.

Acknowledgments:

The research in this proposal was supported by National Natural Science Foundation of China (41773057,42050410319). JM is highly thankful to Chinese Academy of Sciences (CAS) for PIFI. Calculations were run on the TH-2 High Performance Computer System in Lvliang, China.

Bibliography

AMMANN, M. W., BRODHOLT, J. P. & DOBSON, D. P. 2009. DFT study of migration enthalpies in MgSiO3 perovskite. *Physics and Chemistry of Minerals,* 36**,** 151-158.

ARMSTRONG, L. S., WALTER, M. J., TUFF, J. R., LORD, O. T., LENNIE, A. R., KLEPPE, A. K. & CLARK, S. M. 2012. Perovskite Phase Relations in the System CaO-MgO-TiO2-SiO2 and Implications for Deep Mantle Lithologies. *Journal of Petrology,* 53**,** 611-635.

CATALLI, K., SHIM, S.-H., DERA, P., PRAKAPENKA, V. B., ZHAO, J., STURHAHN, W., CHOW, P., XIAO, Y., CYNN, H. & EVANS, W. J. 2011. Effects of the Fe^{3+} spin transition on the properties of aluminous perovskite-New insights for lower-mantle seismic heterogeneities. *Earth and Planetary Science Letters,* 310**,** 293-302.

CREASY, N., GIRARD, J., ECKERT JR, J. O. & LEE, K. K. M. 2020. The Role of Redox on Bridgmanite Crystal Chemistry and Calcium Speciation in the Lower Mantle. 125**,** e2020JB020783.

EBERLE, M., GRASSET, O. & SOTIN, C. 2002. A numerical study of the interaction between the mantle wedge, subducting slab, and overriding plate. *Physics of the Earth and Planetary Interiors,* 134**,** 191-202.

572 FLYVBJERG, H. & PETERSEN, H. G. 1989. Error-estimates on averages of correlated data. *Journal of*
573 *Chemical Physics,* 91**,** 461-466.
574 FUJINO, K., SASAKI, Y., KOMORI, T., OGAWA, H., MIYAJIMA, N., SATA, N. & YAGI, T. 2004. Approach
575 to the mineralogy of the lower mantle by a combined method of a laser-heated diamond
576 anvil cell experiment and analytical electron microscopy. *Physics of the Earth and Planetary*
577 *Interiors,* 143**,** 215-221.
578 FUNAMORI, N., JEANLOZ, R., MIYAJIMA, N. & FUJINO, K. 2000. Mineral assemblages of basalt in the
579 lower mantle. *Journal of Geophysical Research-Solid Earth,* 105**,** 26037-26043.
580 GROCHOLSKI, B., CATALLI, K., SHIM, S.-H. & PRAKAPENKA, V. 2012. Mineralogical effects on the
581 detectability of the postperovskite boundary. *Proceedings of the National Academy of*
582 *Sciences of the United States of America,* 109**,** 2275-2279.
583 GU, T. T., LI, M. M., MCCAMMON, C. & LEE, K. K. M. 2016. Redox-induced lower mantle density
584 contrast and effect on mantle structure and primitive oxygen. *Nature Geoscience,* 9**,** 723-+.
585 HASHIN, Z. & SHTRIKMAN, S. 1963. A VARIATIONAL APPROACH TO THE THEORY OF THE ELASTIC
586 BEHAVIOUR OF MULTIPHASE MATERIALS. *Journal of the Mechanics and Physics of Solids,* 11**,**
587 127-140.
588 HIROSE, K. & FEI, Y. W. 2002. Subsolidus and melting phase relations of basaltic composition in the
589 uppermost lower mantle. *Geochimica Et Cosmochimica Acta,* 66**,** 2099-2108.
590 HIROSE, K., SINMYO, R. & HERNLUND, J. 2017. Perovskite in Earth's deep interior. *Science,* 358**,** 734-
591 738.
592 HIROSE, K., TAKAFUJI, N., SATA, N. & OHISHI, Y. 2005. Phase transition and density of subducted
593 MORB crust in the lower mantle. *Earth and Planetary Science Letters,* 237**,** 239-251.
594 IRIFUNE, T. 1994. ABSENCE OF AN ALUMINOUS PHASE IN THE UPPER PART OF THE EARTHS LOWER
595 MANTLE. *Nature,* 370**,** 131-133.
596 IRIFUNE, T., MIYASHITA, M., INOUE, T., ANDO, J., FUNAKOSHI, K. & UTSUMI, W. 2000. High-pressure
597 phase transformation in CaMgSi2O6 and implications for origin of ultra-deep diamond
598 inclusions. *Geophysical Research Letters,* 27**,** 3541-3544.
599 IRIFUNE, T. & RINGWOOD, A. E. 1993. PHASE-TRANSFORMATIONS IN SUBDUCTED OCEANIC-CRUST
600 AND BUOYANCY RELATIONSHIPS AT DEPTHS OF 600-800 KM IN THE MANTLE. *Earth and*
601 *Planetary Science Letters,* 117**,** 101-110.
602 IRIFUNE, T., SUSAKI, J., YAGI, T. & SAWAMOTO, H. 1989. PHASE-TRANSFORMATIONS IN DIOPSIDE
603 CAMGSI2O6 AT PRESSURES UP TO 25-GPA. *Geophysical Research Letters,* 16**,** 187-190.
604 IRIFUNE, T. & TSUCHIDA, Y. 2007. Mineralogy of the Earth—Phase transitions and mineralogy of the
605 lower mantle. *In:* GD, P. & G, S. (eds.) *Treatise on Geophysics, Vol 2 Mineral Physics.*
606 JUNG, D. Y. & SCHMIDT, M. W. 2011. Solid solution behaviour of CaSiO3 and MgSiO3 perovskites.
607 *Physics and Chemistry of Minerals,* 38**,** 311-319.
608 KAMINSKI, F. 2017. *The Earth's Lower Mantle: Composition and Structure*, Springer International
609 Publishing.
610 KAWAI, K. & TSUCHIYA, T. 2015. Small shear modulus of cubic CaSiO3 perovskite. *Geophysical*
611 *Research Letters,* 42**,** 2718-2726.
612 KESSON, S. E., FITZ GERALD, J. D. & SHELLEY, J. M. 1998. Mineralogy and dynamics of a pyrolite lower
613 mantle. *Nature,* 393**,** 252-255.
614 KOELEMEIJER, P., DEUSS, A. & RITSEMA, J. 2017. Density structure of Earth's lowermost mantle from
615 Stoneley mode splitting observations. *Nature Communications,* 8.
616 KOMABAYASHI, T., HIROSE, K., SATA, N., OHISHI, Y. & DUBROVINSKY, L. S. 2007. Phase transition in
617 CaSiO3 perovskite. *Earth and Planetary Science Letters,* 260**,** 564-569.
618 KRESSE, G. & FURTHMULLER, J. 1996a. Efficiency of ab-initio total energy calculations for metals and
619 semiconductors using a plane-wave basis set. *Computational Materials Science,* 6**,** 15-50.
620 KRESSE, G. & FURTHMULLER, J. 1996b. Efficient iterative schemes for ab initio total-energy
621 calculations using a plane-wave basis set. *Physical Review B,* 54**,** 11169-11186.

KRESSE, G. & JOUBERT, D. 1999. From ultrasoft pseudopotentials to the projector augmented-wave method. *Physical Review B,* 59**,** 1758-1775.

KUPENKO, I., MCCAMMON, C., SINMYO, R., PRESCHER, C., CHUMAKOV, A. I., KANTOR, A., RUEFFER, R. & DUBROVINSKY, L. 2014. Electronic spin state of Fe,Al-containing $MgSiO_3$ perovskite at lower mantle conditions. *Lithos,* 189**,** 167-172.

KURASHINA, T., HIROSE, K., ONO, S., SATA, N. & OHISHI, Y. 2004. Phase transition in Al-bearing CaSiO3 perovskite: implications for seismic discontinuities in the lower mantle. *Physics of the Earth and Planetary Interiors,* 145**,** 67-74.

MARQUARDT, H. & THOMSON, A. R. 2020. Experimental elasticity of Earth's deep mantle. *Nature Reviews Earth & Environment,* 1**,** 455-469.

MATTERN, E., MATAS, J., RICARD, Y. & BASS, J. 2005. Lower mantle composition and temperature from mineral physics and thermodynamic modelling. *Geophysical Journal International,* 160**,** 973-990.

MCNAMARA, A. K. 2019. A review of large low shear velocity provinces and ultra low velocity zones. *Tectonophysics,* 760**,** 199-220.

MICHAEL, P. J. & BONATTI, E. 1985. PERIDOTITE COMPOSITION FROM THE NORTH-ATLANTIC - REGIONAL AND TECTONIC VARIATIONS AND IMPLICATIONS FOR PARTIAL MELTING. *Earth and Planetary Science Letters,* 73**,** 91-104.

MOHN, C. & TRONNES, R. G. 2016. Iron spin state and site distribution in $FeAlO_3$-bearing bridgmanite. *Earth and Planetary Science Letters,* 440**,** 178-186.

MUIR, J. M. R. & BRODHOLT, J. P. 2016. Ferrous iron partitioning in the lower mantle. *Physics of the Earth and Planetary Interiors,* 257**,** 12-17.

O' NEILL, B. & JEANLOZ, R. 1990. EXPERIMENTAL PETROLOGY OF THE LOWER MANTLE - A NATURAL PERIDOTITE TAKEN TO 54 GPA. *Geophysical Research Letters,* 17**,** 1477-1480.

ONO, S. 2008. Experimental constraints on the temperature profile in the lower mantle. *Physics of the Earth and Planetary Interiors,* 170**,** 267-273.

ONO, S., KIKEGAWA, T. & IIZUKA, T. 2004a. The equation of state of orthorhombic perovskite in a peridotitic mantle composition to 80 GPa: implications for chemical composition of the lower mantle. *Physics of the Earth and Planetary Interiors,* 145**,** 9-17.

ONO, S., OHISHI, Y. & MIBE, K. 2004b. Phase transition of Ca-perovskite and stability of Al-bearing Mg-perovskite in the lower mantle. *American Mineralogist,* 89**,** 1480-1485.

PRADHAN, G. K., FIQUET, G., SIEBERT, J., AUZENDE, A. L., MORARD, G., ANTONANGELI, D. & GARBARINO, G. 2015. Melting of MORB at core-mantle boundary. *Earth and Planetary Science Letters,* 431**,** 247-255.

RICOLLEAU, A., PERRILLAT, J.-P., FIQUET, G., DANIEL, I., MATAS, J., ADDAD, A., MENGUY, N., CARDON, H., MEZOUAR, M. & GUIGNOT, N. 2010. Phase relations and equation of state of a natural MORB: Implications for the density profile of subducted oceanic crust in the Earth's lower mantle. *Journal of Geophysical Research-Solid Earth,* 115.

RINGWOOD, A. E. 1991. PHASE-TRANSFORMATIONS AND THEIR BEARING ON THE CONSTITUTION AND DYNAMICS OF THE MANTLE. *Geochimica Et Cosmochimica Acta,* 55**,** 2083-2110.

SHIM, S. H., GROCHOLSKI, B., YE, Y., ALP, E. E., XU, S. Z., MORGAN, D., MENG, Y. & PRAKAPENKA, V. B. 2017. Stability of ferrous-iron-rich bridgmanite under reducing midmantle conditions. *Proceedings of the National Academy of Sciences of the United States of America,* 114**,** 6468-6473.

SHIM, S. H., JEANLOZ, R. & DUFFY, T. S. 2002. Tetragonal structure of CaSiO3 perovskite above 20 GPa. *Geophysical Research Letters,* 29.

SINMYO, R. & HIROSE, K. 2013. Iron partitioning in pyrolitic lower mantle. *Physics and Chemistry of Minerals,* 40**,** 107-113.

STIXRUDE, L., LITHGOW-BERTELLONI, C., KIEFER, B. & FUMAGALLI, P. 2007. Phase stability and shear softening in CaSiO3 perovskite at high pressure. *Physical Review B,* 75.

672 SUN, T., ZHANG, D. B. & WENTZCOVITCH, R. M. 2014. Dynamic stabilization of cubic CaSiO3
673 perovskite at high temperatures and pressures from ab initio molecular dynamics. *Physical*
674 *Review B,* 89**,** 094109-1.
675 TAMAI, H. & YAGI, T. 1989. HIGH-PRESSURE AND HIGH-TEMPERATURE PHASE-RELATIONS IN CASIO3
676 AND CAMGSI2O6 AND ELASTICITY OF PEROVSKITE-TYPE CASIO3. *Physics of the Earth and*
677 *Planetary Interiors,* 54**,** 370-377.
678 THOMSON, A. R., CRICHTON, W. A., BRODHOLT, J. P., WOOD, I. G., SIERSCH, N. C., MUIR, J. M. R.,
679 DOBSON, D. P. & HUNT, S. A. 2019. Seismic velocities of CaSiO3 perovskite can explain
680 LLSVPs in Earth's lower mantle. *Nature,* 572**,** 643-+.
681 TSUCHIYA, T., TSUCHIYA, J., DEKURA, H. & RITTERBEX, S. 2020. Ab Initio Study on the Lower Mantle
682 Minerals. *In:* JEANLOZ, R. & FREEMAN, K. H. (eds.) *Annual Review of Earth and Planetary*
683 *Sciences, Vol 48, 2020.*
684 UCHIDA, T., WANG, Y., NISHIYAMA, N., FUNAKOSHI, K., KANEKO, H., NOZAWA, A., VON DREELE, R. B.,
685 RIVERS, M. L., SUTTON, S. R., YAMADA, A., KUNIMOTO, T., IRIFUNE, T., INOUE, T. & LI, B. S.
686 2009. Non-cubic crystal symmetry of CaSiO3 perovskite up to 18 GPa and 1600 K. *Earth and*
687 *Planetary Science Letters,* 282**,** 268-274.
688 VITOS, L., MAGYARI-KOPE, B., AHUJA, R., KOLLAR, J., GRIMVALL, G. & JOHANSSON, B. 2006. Phase
689 transformations between garnet and perovskite phases in the Earth's mantle: A theoretical
690 study. *Physics of the Earth and Planetary Interiors,* 156**,** 108-116.
691 XU, S. Z., LIN, J. F. & MORGAN, D. 2017. Iron partitioning between ferropericlase and bridgmanite in
692 the Earth's lower mantle. *Journal of Geophysical Research-Solid Earth,* 122**,** 1074-1087.
693 YE, Y., SHIM, S. H., PRAKAPENKA, V. & MENG, Y. 2018. Equation of state of solid Ne inter-calibrated
694 with the MgO, Au, Pt, NaCl-B2, and ruby pressure scales up to 130GPa. *High Pressure*
695 *Research,* 38**,** 377-395.
696 ZHANG, Z., STIXRUDE, L. & BRODHOLT, J. 2013. Elastic properties of MgSiO3-perovskite under lower
697 mantle conditions and the composition of the deep Earth. *Earth and Planetary Science*
698 *Letters,* 379**,** 1-12.

699

700

Figure Captions:

Figure 1: Solubility of Mg in Ca-pv (blue) and Ca in bdg (red) as a function of temperature and pressure (solid lines=25 GPa, dashed=75, dotted=125). The plateau after the graph levels off is the temperature where all ratios of Ca-pv and bdg are miscible into a single phase. This graph is presented with log solubility to demonstrate the low solubility behaviour clearly, a more traditional phase diagram is presented in Figure S3.

Figure 2: Projected T_{mix} for a pyrolytic (Ca#=0.08-0.12), MORB (Ca#=0.3-0.6) and harzburgitic (Ca#=0.01-0.03) composition with no defect elements. In each case the bounds represent the Ca# range with the lower bound of T_{mix} corresponding to the lowest amount of Ca and the higher bound to the highest. Shown on the graph are a lower mantle geotherm (Ono, 2008), the coldest possible slab adiabat (Eberle et al., 2002) and an artificial "hot" geotherm representing hot spots in the lower mantle that is the geotherm+500 K.

Figure 3: Depth at which T_{mix} crosses the A) geotherm or B) "hot" geotherm (geotherm+500 K) for a pyrolytic (Ca#=0.1) mixture with various amounts of Fe and Al as determined via the model outlined in the text. For this model the formation of Fe-Al was prioritised such that Fe-Al forms first and then leftover Fe or Al forms Ferrous iron or Al-Al pairs. Mixing depths above 660 km and below 2900 km have been truncated to these values to follow the lower mantle.

Figure 4: Projected T_{mix} for a pyrolytic mixture with various additional elements. The lines represent Ca#=0.1 while shading represents Ca# bounds between 0.07 and 0.12 which is roughly the Ca# range of pyrolite. Lower Ca# values correspond to lower T_{mix}. Ca# becomes more important as defect elements have a stronger effect on T_{mix}. The "perfect" line represents a defect free mixture. Other lines show different compositions chosen to represent samples of different compositions that could be present and how changing different amounts of element changes the mixing. Fe stands for ferrous iron, Al for Al-Al pairs, Fe-Al for Fe-Al pairs (ferric iron). This plot was constructed by calculating T_{mix} for $CaSiO_3$-$MgSiO_3$ at 25, 75 and 125 GPa and adding in the effect of additional elements as determined in Table 3 (with 75 GPa as the average of 25 and 125 GPa effects) and then fitting a curve to these 3 points. These curves have significant approximations as outlined in the text.

Figure 5: Plot of the change in V_s (solid lines), V_p (dashed lines), V_ϕ (dotted black lines) on converting from a mechanical mixture of Ca-pv and bdg to a single phase calculated directly at Ca#=0.125. These calculations were run at static conditions (~0 K) and 25, 75 and 125 GPa. Ca-pv elasticity was determined in the i4mcm phase, bdg and the mixed phase in the pbnm phase. To determine the elasticity of a mechanical mixture of Ca-pv and bdg we used the Hashin-Shtikman bounds (Hashin and Shtrikman, 1963) which are the bounds pictured, the elasticity change upon mixing must fall between these bounds.

Figure 6: As Figure 5 but showing the variation in elasticity with varied Ca# at 125 GPa.

Tables

Table 1: Change in density on forming a mixed phase for Ca#=0.5 (determined from MD) and 0.125 (extrapolated from MD values at Ca#=0.25 and 0.5) at various pressures and temperatures.

Table 2: Effect of various elements on T_{mix} at 25 and 125 GPa with Ca#=0.10 (Ca#=0.5 and 0.9 values are given in Table S2 and S3) which is a roughly pyrolytic mixture. Columns are name of the element, site at which that element was placed (A=Mg site, B= Si site, AB= 1 element at each, Int=interstitial), the change in ΔH_{mix} in eV from placing one defect element, proportion of this element (K) in the Ca-pv before mixing (1 is all in Ca-pv, 0 is all in bdg) and then the next 3 columns are the change in T_{mix} in K with 0.1, 1 and 10 atomic % (of bridgmanite) of the element in questions. All elements are non-spin polarised except those labelled HS which were run with their standard high spin configuration. 2H represents a water molecule where a Mg has been replaced with 2 Hydrogens in the vacancy. Fe-Al represents a high spin ferric iron replacing a Mg and an Al replacing a Si.

	Ca#=0.125			Ca#=0.5		
	25 GPa	75 GPa	125 GPa	25 GPa	75 GPa	125 GPa
Static	-0.48	-0.41	-0.28	-0.74	-0.75	-0.79
1000 K	-0.15	-0.17	-0.18	-0.59	-0.69	-0.73
2000 K	-0.19	-0.19	-0.19	-0.76	-0.77	-0.75
3000 K	-0.25	-0.23	-0.19	-0.98	-0.93	-0.76

Table 1: Percentage change in density (given to 2 sf) on forming a mixed phase for Ca#=0.5 (determined from MD) and 0.125 (extrapolated from MD values at Ca#=0.25 and 0.5) at various pressures and temperatures.

		25 GPa					125 GPa				
Element	Site	ΔH_{mix}	K	0.10%	1	10	ΔH_{mix}	K	0.10%	1	10
2H	A	0.11	0	2	16	148	0.95	0	13	134	1224
He	Int	-0.27	1	-23	-233	-1883	0.07	1	-7	-70	-628
Ne	Int	-0.86	1	-39	-389	-3453	-0.90	1	-21	-213	-1839
Li(I)	A	0.28	0	6	60	538	0.76	0	11	106	981
Na(I)	A	-0.42	0	-12	-125	-1412	-0.53	0	-9	-86	-883
K(I)	A	-0.10	1	-32	-305	-2057	-0.16	1	-17	-162	-1301
Be(II)	A	0.18	0	3	34	311	1.17	0	17	166	1505
Cu(II)	A	-0.14	0	-5	-51	-526	-0.38	0	-6	-64	-646
Ni(II)	A	-0.39	0	-11	-116	-1292	-0.47	0	-8	-77	-791
Zn(II)	A	-0.13	0	-5	-47	-477	-0.43	0	-7	-71	-722
Co(II)	A	-0.42	0	-12	-124	-1400	-0.55	0	-9	-89	-921
Fe(II)	A	-0.31	0	-9	-95	-1029	-0.48	0	-8	-79	-811
Fe(II)HS	A	-0.20	**0**	**-7**	**-65**	**-682**	**-0.47**	**0**	**-8**	**-76**	**-783**
V(II)	A	-0.26	0	-8	-82	-875	-0.45	0	-7	-74	-761
Cr(II)	A	0.09	0	1	9	82	-0.23	0	-4	-41	-417
Mn(II)	A	0.25	0	5	52	473	0.14	0	1	15	140
Sc(II)	A	-0.22	1	-35	-336	-2244	-0.07	1	-15	-150	-1216
Sc(II) HS	A	-0.26	1	-36	-347	-2313	-0.60	1	-1	-7	-67
Sr(II)	A	0.51	1	-16	-153	-1193	0.70	1	-4	-39	-491
Ba(II)	A	0.98	1	-4	-38	-581	1.38	1	6	57	114
B(III)	AB	0.62	1	15	147	1253	-0.77	1	-12	-123	-1294
Al(III)	AB	0.24	**0**	**5**	**48**	**439**	**0.43**	**0**	**6**	**58**	**550**
Cr(III)	AB	-0.17	1	0	-4	-44	0.07	1	0	5	44
Cr(III)Hs	AB	0.14	1	2	23	218	-0.15	1	-3	-29	-289
Ga(III)	AB	0.13	0	2	20	185	0.34	0	4	44	419
Fe(III)	AB	0.79	0	19	188	1569	1.03	0	15	146	1337
Fe(III)HS	AB	0.01	**0**	**-1**	**-10**	**-96**	**0.18**	**0**	**2**	**20**	**189**
Sc(III)	AB	-0.20	0	-6	-65	-673	-0.07	**0**	-2	-17	-167
In(III)	AB	-0.07	0	-3	-32	-322	0.17	0	2	19	182
Fe-Al	AB	0.02	**0**	**-1**	**-7**	**-74**	**0.00**	**0**	**-1**	**-7**	**-71**
C 4+	B	-0.51	1	-15	-148	-1753	-0.08	0	-2	-19	-193
S 4+	B	-0.45	0	-13	-133	-1530	-0.21	0	-4	-38	-387
Ge4+	B	-0.17	0	-6	-57	-587	-0.09	0	-2	-20	-204
Sn4+	B	-0.51	0	-15	-150	-1780	-0.38	0	-6	-63	-645
Ti4+	B	-0.07	1	-3	-32	-329	-0.26	0	-4	-45	-452

Table 2: Effect of various elements on T_{mix} at 25 and 125 GPa with Ca#=0.1 (Ca#=0.5 and 0.9 values are in Table S6 and S7) which is a roughly pyrolytic mixture. Columns are name of the element, site at which that element was placed (A=Mg site, B= Si site, AB= 1 element at each, Int=interstitial), the change in ΔH_{mix} in eV from placing one defect element, proportion of this element (K) in the Ca-pv before mixing (1 is all in Ca-pv, 0 is all in bdg) and then the next 3 columns are the change in T_{mix} in K with 0.1, 1 and 10 atomic % (of bridgmanite) of the element in questions. All elements are non-spin polarised except those labelled HS which were run with their standard high spin configuration. 2H

765 represents a water molecule where a Mg has been replaced with 2 Hydrogens in the vacancy. Fe-Al
766 represents a high spin ferric iron replacing a Mg and an Al replacing a Si.

767

Figure 1

Click here to access/download;Figure;Figure1.pdf

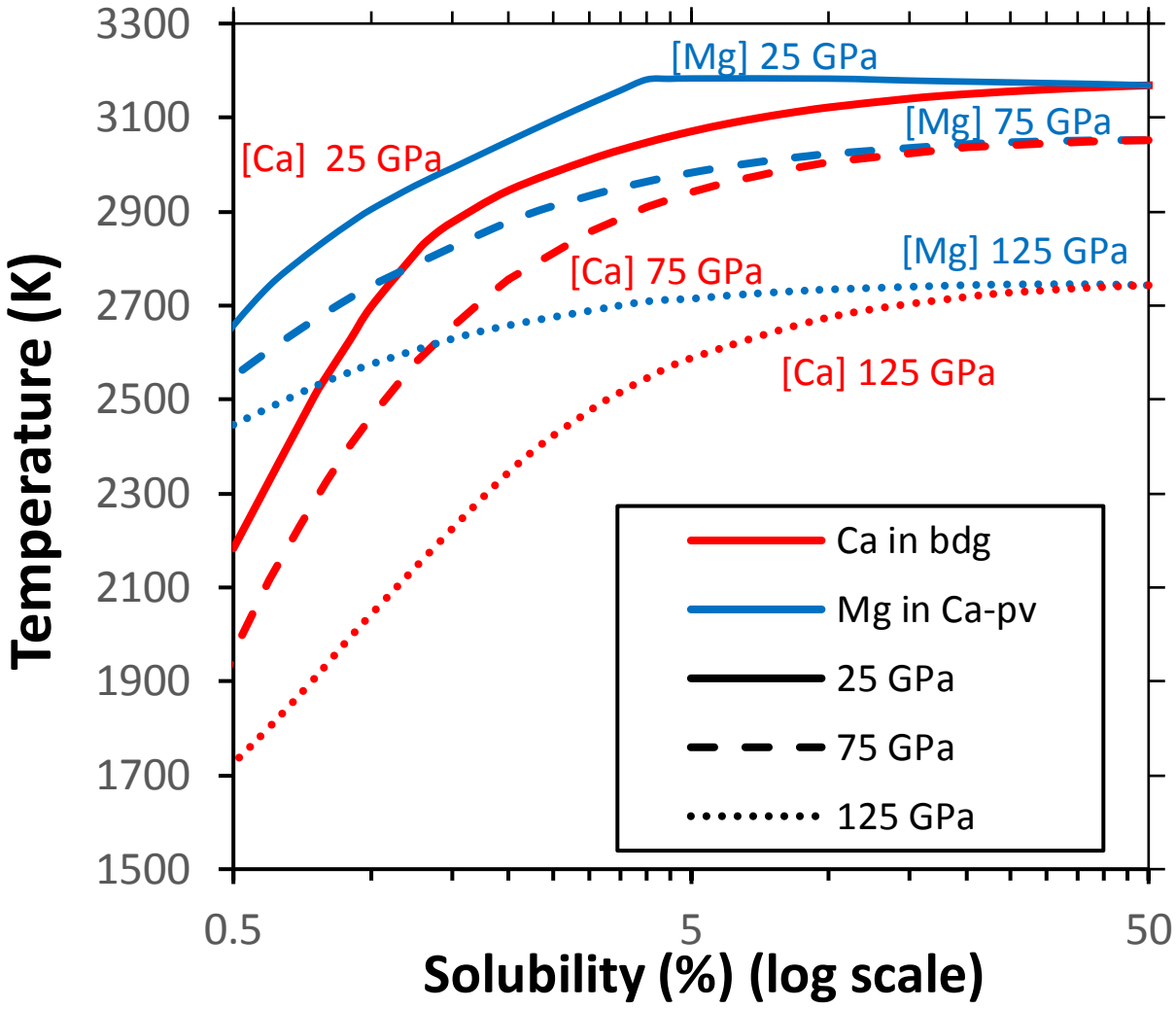

Figure 2

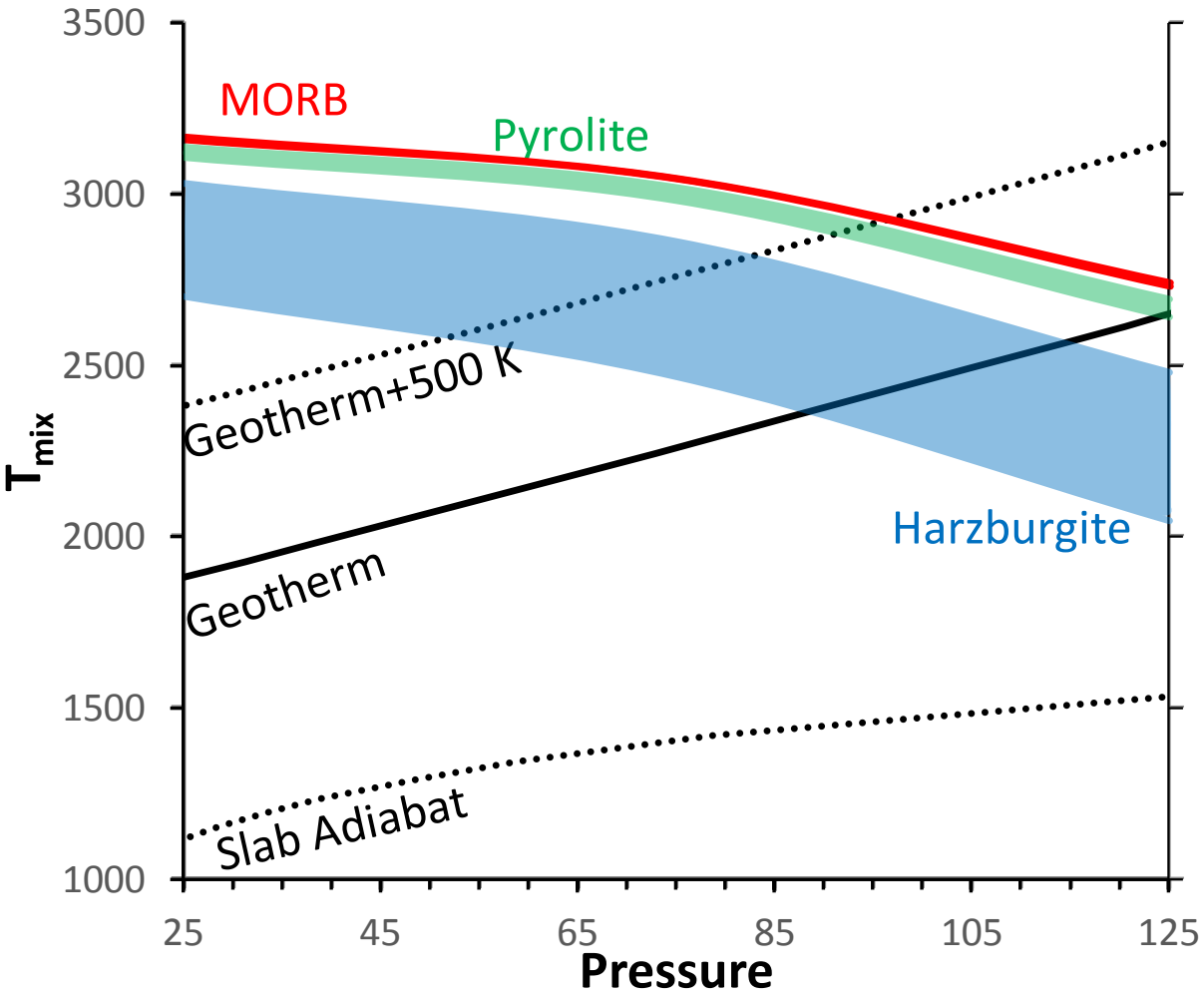

Figure 3

Click here to access/download;Figure;Figure3.pdf

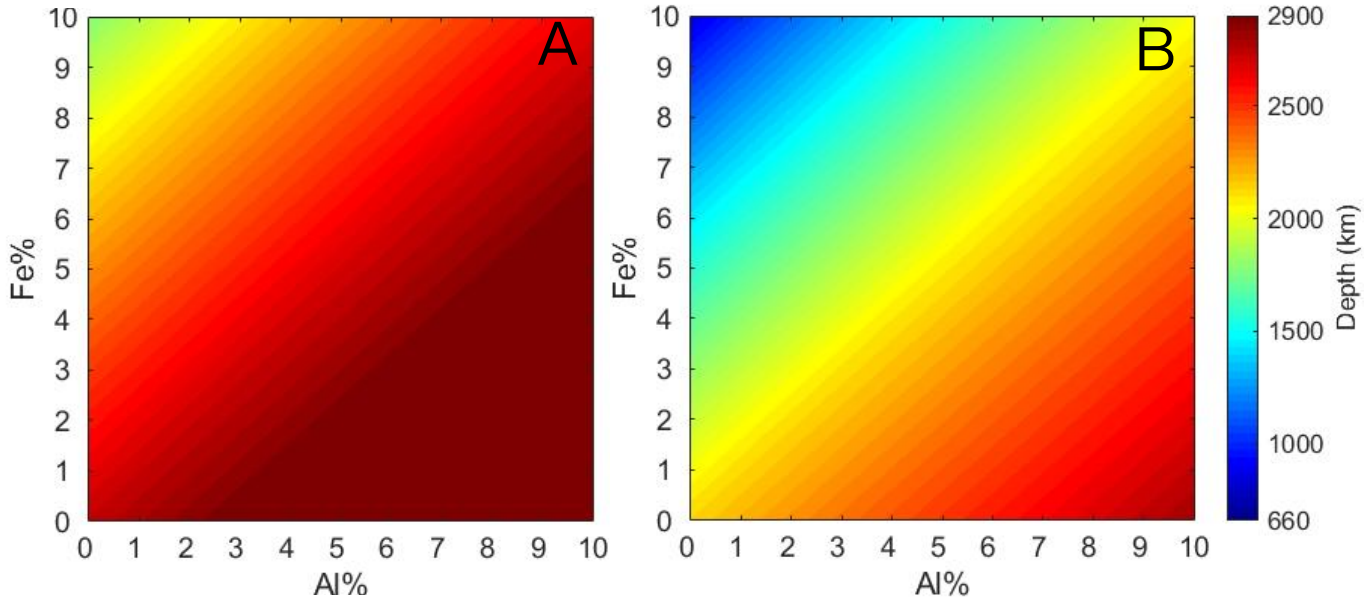

Figure 4

Click here to access/download;Figure;Figure4.pdf

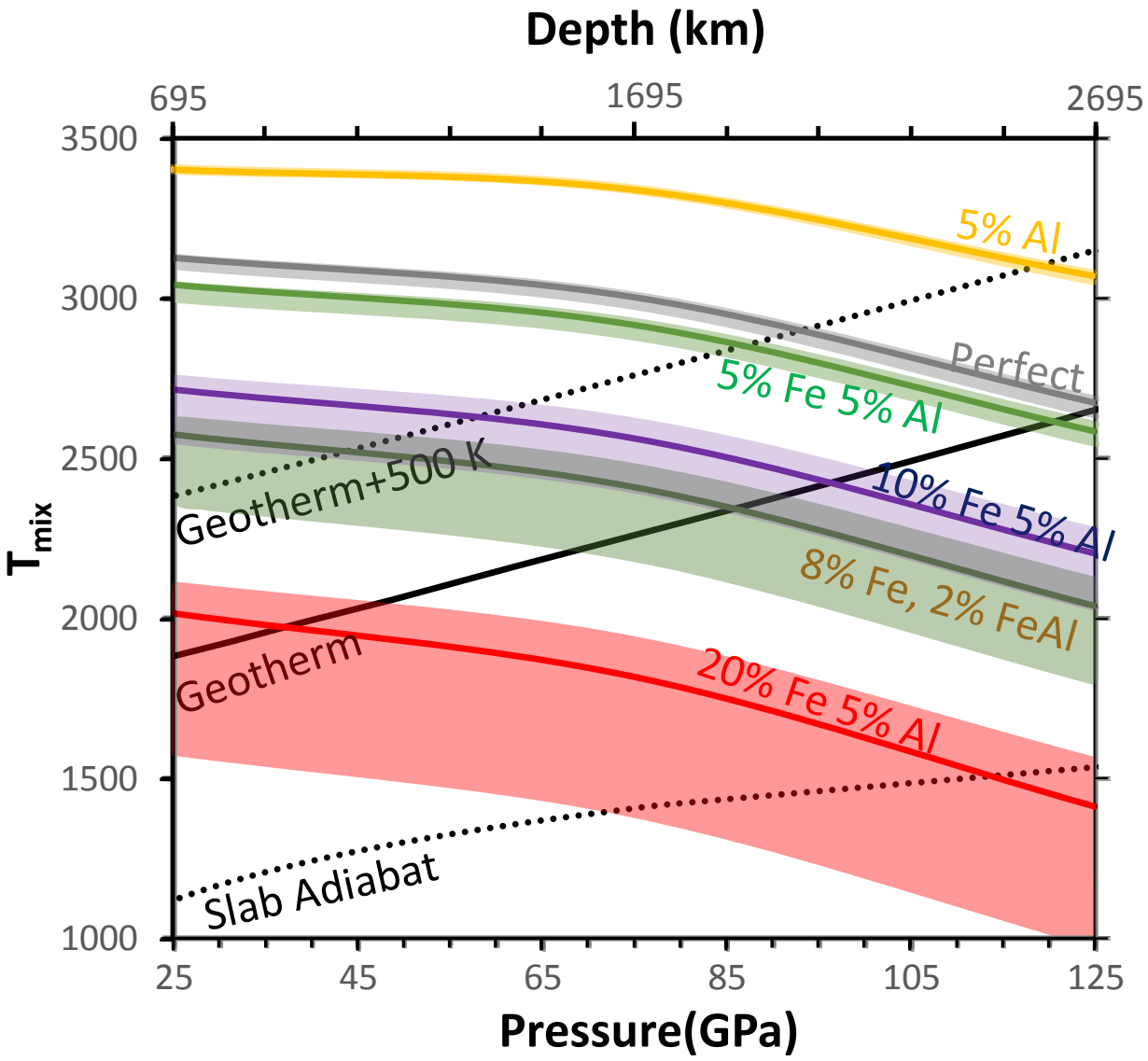

Figure 5

Click here to access/download;Figure;Figure5.pdf

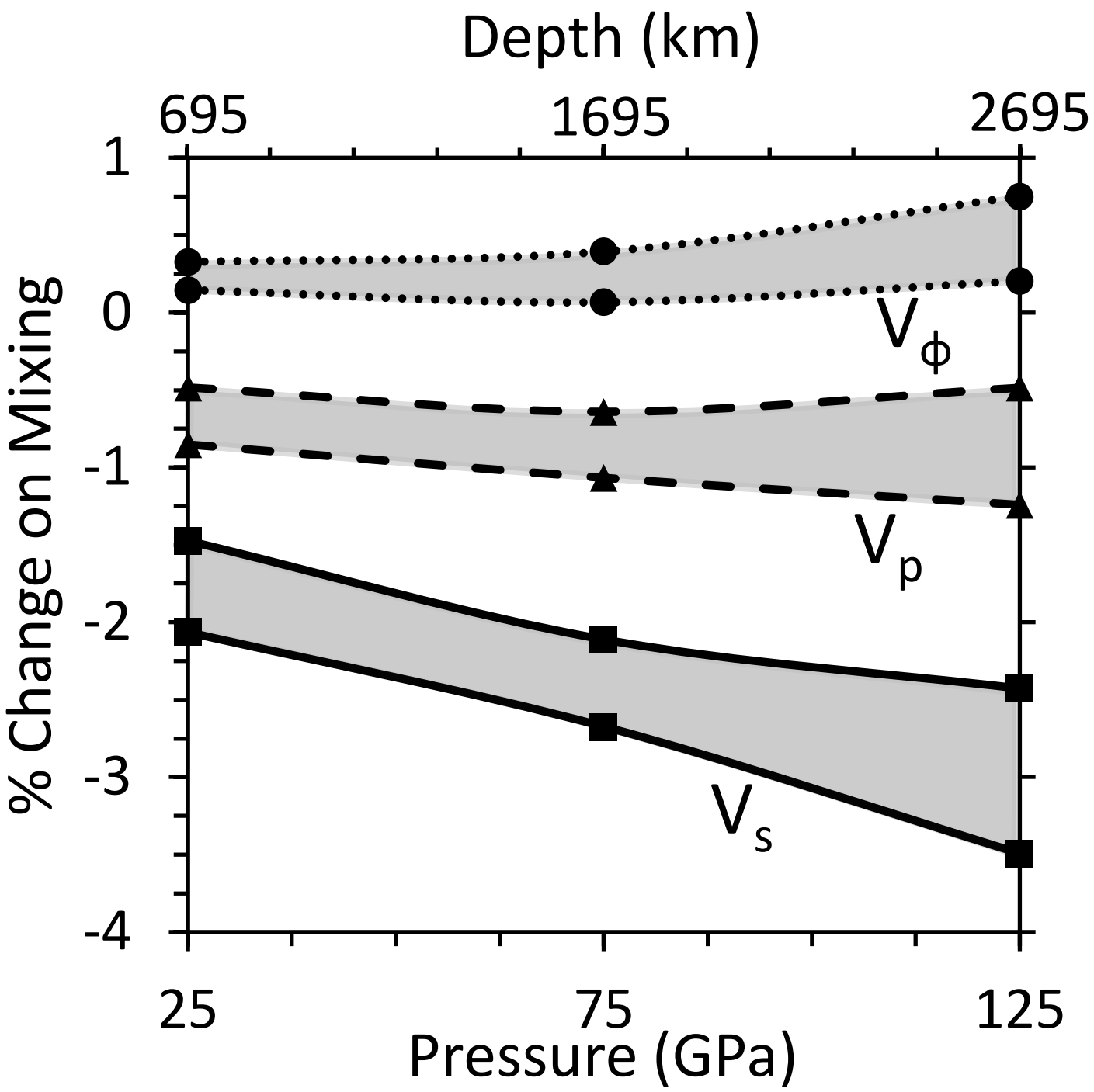

Figure 6

Click here to access/download;Figure;Figure6.pdf